information

Article

Using an Improved Regularization Method and Rigid Transformation for Super-Resolution Applied to MRI Data

Matina Christina Zerva, Giannis Chantas and Lisimachos Paul Kondi *

Department of Computer Science and Engineering, University of Ioannina, 451 10 Ioannina, Greece; s.zerva@uoi.gr (M.C.Z.); gchantas@uoi.gr (G.C.)
* Correspondence: lkon@uoi.gr

Abstract: Super-resolution (SR) techniques have shown significant promise in enhancing the resolution of MRI images, which are often limited by hardware constraints and acquisition time. In this study, we introduce an advanced regularization method for MRI super-resolution that integrates spatially adaptive techniques with a robust denoising process to improve image quality. The proposed method excels in preserving high-frequency details while effectively suppressing noise, addressing common limitations of conventional SR approaches. The validation of clinical MRI datasets demonstrates that our approach achieves superior performance compared to traditional algorithms, yielding enhanced image clarity and quantitative improvements in metrics such as the peak signal-to-noise ratio (PSNR) and structural similarity index (SSIM).

Keywords: MRI; super-resolution; regularization method

Citation: Zerva, M.C.; Chantas, G.; Kondi, L.P. Using an Improved Regularization Method and Rigid Transformation for Super-Resolution Applied to MRI Data. *Information* **2024**, *15*, 770. https://doi.org/10.3390/info15120770

Academic Editors: Mingfeng Jiang, Hongfu Sun, Lijun Lu and Zhifeng Chen

Received: 14 October 2024
Revised: 26 November 2024
Accepted: 29 November 2024
Published: 3 December 2024

1. Introduction

Super-resolution (SR) has gained significant attention in recent years, particularly in medical imaging applications, where the resolution of acquired images is often limited by hardware constraints, time limitations, and patient comfort considerations. Traditional medical imaging modalities such as Magnetic Resonance Imaging (MRI) and Computed Tomography (CT) produce images at a resolution that can restrict the level of detail observable for diagnostic purposes. Increasing the resolution of these images through hardware improvements is often costly and impractical. As a result, computational techniques like SR have emerged as a powerful alternative, allowing high-resolution (HR) images to be reconstructed from low-resolution (LR) inputs without the need for expensive hardware [1–3].

The principle behind SR methods is to overcome limitations by leveraging redundant information from multiple LR images or sequences, often involving complex algorithms like regularization methods and machine learning models [4]. Various approaches, from classic interpolation methods to more advanced neural-network-based models, have been employed to enhance the quality of medical images in terms of spatial resolution, signal-to-noise ratio (SNR), and edge preservation [5].

In medical imaging, SR is particularly valuable because it enhances the quality of images used in diagnostic processes. For instance, MRI scans are used to assess various medical conditions, and improving their resolution can lead to more accurate diagnoses. Using SR techniques like Wiener filter regularization [1] or edge-preserving high-frequency regularization [3] allows for better visual quality in images without increasing acquisition costs or hardware requirements. Furthermore, neural-network-based SR methods [2] have demonstrated promising results in improving image quality with reduced computational time, making them suitable for real-time applications in clinical settings.

The concept of SR in medical imaging has evolved significantly over the years, with various methodologies proposed to tackle the challenges of resolution enhancement. One of the early applications of SR to MRI was proposed by Peled et al. [6], where an Iterative

Back-Projection (IBP) method was used to enhance MRI images of human white matter fiber tracts. While this method shows some promise, it was limited by the use of synthetic image data, which do not fully capture the complexities of real-world medical imaging. Subsequent work by Scheffler [7] addressed this limitation by highlighting the importance of utilizing original image data for more reliable SR reconstruction.

More recently, the integration of machine learning techniques into SR models has shown great promise. For example, a method combining iterative regularization with feed-forward neural networks was proposed by Babu et al. [2], yielding improved results over previous methods due to its capability of handling noise and producing clearer, higher-resolution images. This method demonstrates the potential of neural networks to enhance SR models by reducing computational complexity while maintaining high image quality.

Bayesian methods have also been a major area of exploration in SR research [8–12]. Aguena et al. [1] introduced a Bayesian approach to MRI SR, which employed a Wiener filter to regularize the iterative solution. This method achieved notable improvements in both noise reduction and edge preservation. Similarly, Ben-Ezra et al. [4] proposed a regularized SR framework for brain MRI, incorporating domain-specific knowledge to improve the quality of SR reconstructions. Their approach outperformed traditional maximum a posteriori (MAP) estimators in terms of both edge clarity and overall image quality.

Moreover, Ahmadi and Salari [3] proposed a high-frequency regularization technique that combines edge-preserving methods with traditional SR models. Their approach allows for enhanced edge definition in MRI images without the need for image segmentation, offering a computationally efficient solution suitable for clinical applications.

The Accelerated Proximal Gradient Method (APGM), as outlined in ref. [13], is a well-known optimization technique commonly used for solving inverse problems in imaging, including SR. APGM accelerates the convergence of proximal gradient methods, which are widely adopted for SR tasks involving regularization. Its primary strength lies in its speed, as it converges more quickly than traditional gradient methods, making it suitable for large-scale imaging problems. However, APGM's effectiveness is heavily dependent on the choice of regularizer, which influences how well the method can balance smoothness and sharpness in the reconstructed image. Poorly chosen regularizers can introduce artifacts or excessively smooth the image. While APGM is flexible and powerful, it requires careful tuning to achieve optimal results, especially when handling high-frequency details.

Block matching and 3D filtering (BM3D), a renowned denoising algorithm discussed in ref. [14], uses a collaborative filtering approach to reduce noise while preserving image structures. For super-resolution tasks, BM3D can act as a regularizer that effectively manages noise without compromising edges and textures. Its block-matching mechanism compares similar patches in the image, applying 3D filtering to reduce noise in these matched blocks. Although BM3D excels at preserving textures and fine details in natural images, its computational complexity can be high, particularly when dealing with large images or complex noise patterns. Additionally, the block-matching process may struggle in scenarios where image structures do not align well with the blocks, leading to potential loss of detail in areas with intricate textures.

Gu et al. [15] enhanced the BM3D algorithm by introducing weighted nuclear norm minimization, which improved its performance in image denoising. This modification further solidified BM3D as a versatile and widely adopted tool in image processing. Although BM3D is primarily an image-denoising algorithm rather than a typical regularization technique, denoising often relies on regularization to reduce noise and improve image quality. BM3D utilizes collaborative filtering and 3D-transform-domain techniques to achieve denoising, making it more aligned with advanced signal processing than conventional regularization methods.

Total variation (TV) regularization, a widely used technique in inverse problems, aims to promote sparsity in image gradients, leading to smoother regions while preserving sharp edges. TV regularization is known for its simplicity and its ability to retain edge information, making it a popular choice in SR tasks. However, TV regularization often suffers from the staircasing effect, where smooth regions of the image appear blocky or exhibit artificial edges. Over-regularization can further result in a loss of fine details, which limits the technique's applicability in images with rich textures or high-frequency content [16].

Rapid and Accurate Image Super-Resolution (RAISR), introduced in ref. [17], is a learning-based SR method that is both computationally efficient and fast. It works by learning filters that are adaptive to local image features, such as gradients and edge orientations. Unlike deep-learning-based methods that often require significant computational resources, RAISR is lightweight and quick, making it an attractive option for real-time applications. Despite its efficiency, RAISR tends to fall short when compared to more advanced SR methods like deep neural networks in terms of recovering high-frequency details. Its performance is highly dependent on the quality of the learned filters, and it may struggle with images that have complex structures or varying noise levels.

PPPV1, as described in ref. [18], is a video super-resolution method, based on the Plug-and-Play (PnP) framework. This method iteratively refines images, ensuring the gradual recovery of fine details over multiple iterations. A key feature of PPPV1 is its reliance on a denoising module, originally based on DnCNN (Denoising Convolutional Neural Network), to remove noise from the image during each step of the reconstruction process. While DnCNN is effective at reducing noise, it sometimes introduces oversmoothing, especially in high-frequency regions where texture and fine details are critical. The proposed improvement to this method involves replacing DnCNN with a custom prior for denoising. This change allows for more control over detail preservation and texture recovery, potentially reducing the risk of oversmoothing. A well-designed custom prior can provide a better balance between noise suppression and sharpness, which could lead to more accurate and visually appealing results, particularly in areas with intricate patterns or high-frequency details.

In addition to neural-network-based and Bayesian approaches, convex optimization methods have been explored. Kawamura et al. [5] applied convex optimization techniques to MRI SR, producing state-of-the-art results by carefully balancing noise suppression and detail preservation.

Overall, the field of SR in medical imaging is rapidly advancing, with numerous approaches showing great potential in improving diagnostic imaging and reducing the need for high-cost imaging hardware. The next phase of research will likely focus on integrating these various techniques into more robust, real-time systems suitable for clinical environments.

In this paper, we propose an improved PPP regularization method for MRI super-resolution, utilizing an effective prior specifically designed for denoising and handling motion between frames. Building upon the foundation of our previous method (PPPV1 [18]), our approach incorporates an innovative denoiser that significantly enhances performance. Unlike traditional methods that primarily focus on denoising, our method integrates these advances into an MRI super-resolution framework.

2. Materials and Methods

The acquisition model we are assuming is

$$\mathbf{y} = A\mathbf{x} + \varepsilon, \tag{1}$$

where

- $\mathbf{y}$ is the full set of low resolution (LR) frames, described as $\mathbf{y} = [\,\mathbf{y}_1{}^T, \mathbf{y}_2{}^T, \ldots, \mathbf{y}_p{}^T]\,^T$, where $\mathbf{y}_k$, $k = 1, 2, \ldots, p$ are the p LR images. Each observed LR image is of size $N_1 \times N_2$. Let the kth LR image be denoted in lexicographic notation as $\mathbf{y}_k = [\,y_{k,1}, y_{k,2}, \ldots, y_{k,M}]\,^T$, for $k = 1, 2, \ldots, p$ and $M = N_1 N_2$.
- $\mathbf{x}$ is the desired high-resolution (HR) image, of size $L_1 N_1 \times L_2 N_2$, written in lexicographical notation as the vector $\mathbf{x} = [\,x_1, x_2, \ldots, x_N]\,^T$, where $N = L_1 N_1 L_2 N_2$

and L_1 and L_2 represent the up-sampling factors in the horizontal and vertical directions, respectively.

- $\varepsilon = [\,\varepsilon_1, \varepsilon_2, \ldots, \varepsilon_p\,]^T$, where ε_k is the noise vector for frame k and contains independent zero-mean Gaussian random variables.
- $A = [\,A_1, A_2, \ldots, A_p\,]^T$ is the degradation matrix, which performs the operations of blur, rigid transformation and subsampling.

Assuming that each LR image is corrupted by additive noise, we can then represent the observation model as [19]

$$\mathbf{y}_k = A_k\mathbf{x} + \varepsilon_k \text{ for } 1 \le k \le p \tag{2}$$

where

$$A_k = SB_kM_k. \tag{3}$$

M_k is a matrix of size $L_1N_1L_2N_2 \times L_1N_1L_2N_2$ that performs the rigid transformation, B_k represents a $L_1N_1L_2N_2 \times L_1N_1L_2N_2$ blur matrix, and S is a $N_1N_2 \times L_1N_1L_2N_2$ subsampling matrix. In our case, $B_k = I$, since we assumed no added blur on video frames.

The goal is to find the estimate $\hat{\mathbf{x}}$ of the HR image $\mathbf{x}$ from the p LR images y_k by minimizing the cost function

$$\hat{\mathbf{x}} = \arg\min_{\mathbf{x}\in\mathbb{R}^N} f(\mathbf{x}) \text{ with } f(\mathbf{x}) = g(\mathbf{x}) + h(\mathbf{x}), \tag{4}$$

where $g(\mathbf{x}) = \sum_{k=1}^{p} \frac{1}{2}\|A_k\mathbf{x} - \mathbf{y}_k\|_2^2$ is the "fidelity to the data" term, and $h(\mathbf{x})$ is the regularization term, which offers some prior knowledge about $\mathbf{x}$. In this study, we adopt the Plug-and-Play priors approach, in which the ADMM (Alternating Direction Method of Multipliers) algorithm is modified so that the proximal operator related to $h(\mathbf{x})$ is replaced by a denoiser that solves the problem of Equation (5). The denoiser used is based on the work by Chantas et al. [20].

The following outlines the algorithm we propose:

1. The first step of our algorithm is to evaluate the term M_k from the Equation (3), by using rigid registration. Rigid registration, also known as rigid body registration or rigid transformation, is a fundamental technique in medical image processing and computer vision. It is used to align two images by performing translations and rotations while preserving the shape and size of the structures within the images [21]. In a 2D plane, a rigid transformation can be represented using a 3×3 matrix, often referred to as the transformation matrix. For example, a 2D translation can be represented as [22]

$$T = \begin{bmatrix} 1 & 0 & t_x \\ 0 & 1 & t_y \\ 0 & 0 & 1 \end{bmatrix}$$

   Rotation and reflection matrices can also be formulated similarly. The result of the rigid transformation is represented as an affine transformation matrix. This matrix captures the translation and rotation parameters applied to the original image [22]. We assume that one of the LR images, $\mathbf{y}_{mid}$ (typically the middle one), is produced from the HR image $\mathbf{x}$ by applying only downsampling, without transformation. Thus, $M_{mid} = I$. Rigid transformation is calculated between $\mathbf{y}_{mid}$ and the rest of the LR images. Following that, we obtain M_k for the remaining $p-1$ images.
2. The subsequent phase is centered on employing the PnP-ADMM technique. We execute the PnP-ADMM, adhering to the procedure outlined in Algorithm 1, until reaching convergence, in order to minimize the problem described by Equation (4). The initial HR image guess, $\mathbf{x}^0$, is generated from $\mathbf{y}_{mid}$ using the pseudo-inverse of $\mathbf{A}_{mid}$. Here, D represents the denoising operator, introduced and discussed in Section 2.1, and g is formulated as $g(\mathbf{x}) = \sum_{k=1}^{p} \frac{1}{2}\|A_k\mathbf{x} - \mathbf{y}_k\|_2^2$.

Algorithm 1 PnP -ADMM [23]

1: $\mathbf{u}^0 = \mathbf{0}, \mathbf{x}^0$, and $\gamma > 0$
2: **for** $k = 1, 2, \ldots, t$ **do**
3: $\quad \mathbf{z}^k \leftarrow prox_{\gamma g}(\mathbf{x}^{k-1} - \mathbf{u}^{k-1})$
4: $\quad \mathbf{x}^k \leftarrow D(\mathbf{z}^k + \mathbf{u}^{k-1})$
5: $\quad \mathbf{u}^k \leftarrow \mathbf{u}^{k-1} + (\mathbf{z}^k - \mathbf{x}^k)$
6: **end for**
7: **return** $\mathbf{x}^t$

We next explain the modification made to the standard ADMM algorithm to obtain PnP-ADMM. Line 4 or the standard ADMM is $\mathbf{x}^k \leftarrow prox_{\beta h}(\mathbf{z}^k + \mathbf{u}^{k-1})$. In the PnP-ADMM, the proximal operator is replaced by a denoiser D that solves the problem

$$\mathbf{z} = \mathbf{x}_0 + \mathbf{w}, \text{ where } \mathbf{x}_0 \sim p, \mathbf{w} \sim N(0; \beta I). \tag{5}$$

It can be shown that the Maximum A Posteriori (MAP) estimator $\hat{\mathbf{x}_0}$ of $\mathbf{x}_0$ is the proximal operator:

$$\hat{\mathbf{x}_0} = prox_{\beta h}(\mathbf{z}) = \arg\min_{\mathbf{x} \in \mathbb{R}^N} \{\frac{1}{2}\|\mathbf{x} - \mathbf{z}\|_2^2 \, + \beta h(\mathbf{x})\}, \tag{6}$$

for $h(\mathbf{x}) = -\log(p(\mathbf{x}))$.

2.1. The Denoising Algorithm

In this section, we describe the algorithm we use to implement the denoising step of Equation (6). The algorithm is a simplification of that proposed in ref. [20], and it is formulated in a probabilistic (Variational Bayes) context and utilizes an effective prior distribution, which we describe in short next.

2.1.1. The Prior Distribution

The prior distribution we employ for the denoising step was proposed in ref. [20] for single-image Super-Resolution, and it is of the form

$$p(\mathbf{x}) \propto \prod_{w \in \Omega} \left(\sum_{\delta \in \mathcal{D}} \left(1 + \frac{\lambda}{\nu} \epsilon_{w,\delta}(\mathbf{x}) \right)^{-\frac{\nu+1}{2}} \right), \tag{7}$$

where λ, ν are the real-positive distribution parameters and $\boldsymbol{\epsilon}_{w,\delta}$ is a similarity measure between two patches, each with a center pixel w and $w + \delta$. The above distribution is produced after integrating out the hidden variables of the prior in ref. [20]. However, this form is never explicitly used (it is not necessary) in the optimization algorithm. We show it here in this form for simplicity of presentation. Indeed, $h(\mathbf{x})$ enables us to interpret the prior in a deterministic context, analogous to the penalty function imposed on the video frames; see Equation (6).

We introduce a similarity measure between two image patches, denoted as $\mathcal{N}_w$ and $\mathcal{N}_{w'}$, where $\mathbf{x}(w)$ and $\mathbf{x}(w')$ represent the central pixel of the first and second patch, respectively.

The complete set of pixel coordinates is represented by $\Omega = \{1, \ldots, N\}$. Furthermore, we define δ as the integer displacement between the center pixels of the two patches, such that $w' = w + \delta$. For measuring similarity, we employ a weighted Euclidean norm, represented by $\epsilon_{w,\delta}$, to quantify the difference between $\mathcal{N}_w$ and $\mathcal{N}_{w'}$ (or $\mathcal{N}_{w+\delta}$) as follows:

$$\epsilon_{w,\delta} = \sum_{i \in \Omega} \mathbf{v}_\delta^2(i) \mathbf{g}_w(i), \tag{8}$$

where $\mathbf{v}_\delta$ is defined by $\mathbf{v}_\delta = \mathbf{Q}_\delta \mathbf{x}$ and $\mathbf{v}_\delta^2$ indicates the vector obtained by squaring each element of $\mathbf{v}_\delta$. $\mathbf{Q}_\delta$ represents the difference operator, an $N \times N$ matrix, such that the i-th component of $\mathbf{Q}_\delta \mathbf{x}$ equals $\mathbf{x}(i) - \mathbf{x}(i')$ for all $i, i' \in \Omega$ with $i' - i = \delta$. The matrix $\mathbf{G}_w$ is an $N \times N$ diagonal matrix, where its diagonal elements corresponding to the pixels in $\mathcal{N}_w$ are the only non-zero values, specifically, $\mathbf{G}_w(i,i) = 0$, for all i not in $\mathcal{N}_w$. Lastly, we denote by $\mathbf{g}_w$ the $N \times 1$ vector with elements being the weights of the weighted norm: the closer to the central pixel of the patches, the larger the weight value.

The norm defined by (8) retains its value even if the summation (8) runs over only the subset $\mathcal{N}_w \subset \Omega$ instead of Ω, since $\mathbf{g}_w(i) = 0$ for $i \notin \mathcal{N}_w$. However, we use the full summation range over Ω for enabling fast computations with the Fast Fourier Transform, as explained next.

The distance between the patch $\mathcal{N}_{w=1}$ and an arbitrary patch $\mathcal{N}_{w'}$, $w' \in \Omega$, is $\delta = w - w' = 1 - w'$. Given that the image patches correspond to $\mathbf{g}_1$ and $\mathbf{g}_{w'}$, it is

$$\mathbf{g}_{w'}(i) = \mathbf{g}_{w=1}(i - \delta) = \mathbf{g}_1(i + 1 - w), \ \forall i \in \Omega. \tag{9}$$

As we can see, each $\mathbf{g}_{w'}$ is a circularly shifted by w' version of $\mathbf{g}_1 \equiv \mathbf{g}$ (denoted simply by $\mathbf{g}$ from now on). The Formula (8) for calculating $\epsilon_{w,\delta}$, expressed in terms of $\mathbf{g}$, is

$$\epsilon_{w,\delta} = \sum_{i \in \Omega} \mathbf{v}_\delta^2(i) \mathbf{g}_w(i) = \sum_{i \in \Omega} \mathbf{v}_\delta^2(i) \mathbf{g}(i + 1 - w). \tag{10}$$

Clearly, the values of $\epsilon_{w,\delta}$ for all w's are the result of the *correlation* between $\mathbf{v}_\delta^2$ and $\mathbf{g}$, since the indices of $\mathbf{v}^2$ and $\mathbf{g}$ always differ by the constant $1 - w$. To calculate the correlation required for the super-resolution technique discussed in the following section, we use the Fast Fourier Transform (FFT). This approach decreases the computational complexity of the algorithm from $O(N^2)$, typical for correlation calculations, to $O(N \log N)$, which is the complexity for multiplication in the DFT (Discrete Fourier Transform) domain.

2.1.2. Denoising in PnP-ADMM

Next, we describe the algorithm we employ in the PnP-ADMM context of Algorithm 1, and specifically for the denoising step (line 4). The algorithm we employ, as a denoising subproblem of the general super-resolution algorithm (Algorithm 1), is in essence a special case of the VBPS algorithm in ref. [20], where there is no blurring or decimation. Mathematically speaking, this means that the imaging operator $\mathbf{DH}$ is the $N \times N$ identity matrix $\mathbf{I}$, as shown in line 8 of Algorithm 2.

More specifically, the imaging model assumed for the denoising step is a simplified form of Equation (2.1) in ref. [20], because it is now $\mathbf{DH} = \mathbf{I}$ (i.e., no blur/decimation, so it is just the identity matrix). Also, in this form, $\mathbf{z}^k + \mathbf{u}^{k-1}$ has the role of the "noisy image" and $\mathbf{x}^k$ is the uncorrupted one, meant to be estimated by the denoising algorithm.

Algorithm 2 is the result of the adoption of both the imaging model mentioned above and the prior (5) for $\mathbf{x}$. Lastly, note that the denoising Algorithm 2 selects, automatically, in the initialization step, the noise variance β, among other parameters.

Algorithm 2 Variational Bayes Patch Similarity Denoising

Input: Noisy image $\mathbf{z}^k + \mathbf{u}^{k-1}$.
Output: Denoised image $\mathbf{x}^k$.

Initialization:
Image initial estimate: Set $\alpha_{\text{new}} = \alpha/2$, where α is the regularization parameter obtained from [24]. Then, set $\mathbf{m}^{(0)} = \mathbf{x}_{\text{Stat}}$, where $\mathbf{x}_{\text{Stat}}$ is the super-resolved image obtained after setting $\alpha = \alpha_{\text{new}}$. *Parameter selection*: Set $t = 0$, and $\beta = N / \|\mathbf{x} - \mathbf{z}\|_2^2$, $\lambda = 10^3 \alpha_{\text{new}}$, $\nu = 7$, $rmax = 280$, MAXITER $= 25$ and err$= 10^{-7}$.

Algorithm 2 *Cont.*

while $\|\mathbf{m}^{(t)} - \mathbf{m}^{(t-1)}\|_2^2 / N > err$ AND $t <$ MAXITER **do**
  for every δ in $\mathcal{D}$ **do**
    $\mathbf{v}_\delta \leftarrow \mathbf{Q}_\delta \mathbf{m}^{(t)}$
    for every w in Ω **do**
      Calculate the expectations of the following model's random variables:

$$\langle a_{w,\delta} \rangle_{(t)} = \frac{1+\nu}{\lambda \hat{\epsilon}_{w,\delta} + \nu},$$

$$\langle z_{w,\delta} \rangle_{(t)} = \frac{e^{-\frac{\lambda}{2} \langle a_{w,\delta} \rangle_{(t)} \hat{\epsilon}_{w,\delta} - \frac{\nu}{2} \log \langle a_{w,\delta} \rangle_{(t)}}}{\sum_\delta e^{-\frac{\lambda}{2} \langle a_{w,\delta'} \rangle_{(t)} \hat{\epsilon}_{w,\delta'} - \frac{\nu}{2} \log \langle a_{w,\delta'} \rangle_{(t)}}},$$

      where $\hat{\epsilon}$ is the ϵ in (8), calculated with the image estimation provided in the previous iteration $t-1$,
      calculate $\mathbf{b}_\delta^{(t)}(w) = \langle a_{w,\delta} \rangle_{(t)} \langle z_{w,\delta} \rangle_{(t)}$, for all w and δ,
      set $\mathbf{\Lambda}_\delta^{(t)} = \text{diag}\{\mathbf{b}_\delta^{(t)} * \mathbf{g}\}$ (convolution),
      $t \leftarrow t+1$
      Obtain $\mathbf{m}^{(t)}$ by solving the linear system $\left(\beta \mathbf{I} + \lambda \sum_\delta \mathbf{Q}_\delta^T \Lambda_\delta^{(t)} \mathbf{Q}_\delta\right) \mathbf{m}^{(t)} = \beta \mathbf{y}$ with the Conjugated Gradients algorithm.
    end for
  end for
end while
T = t; $\mathbf{x}^k = \mathbf{m}^{(T)}$.

We implemented our method in SCICO [25], which is an open-source library for computational imaging that includes implementations of several algorithms. We used the main ADMM code implementation from SCICO, which we modified to take into consideration rigid transformation and to use our custom prior.

To evaluate our method, the widely used publicly available dataset named the cancer image archive (TCIA) [26] was used in order to compare our results to the previously proposed method. Specifically, we conducted experiments using a dataset of LR brain MRI images and a corresponding HR reference dataset.

3. Results

The datasets used in this study were obtained from the Cancer Imaging Archive, focusing on two distinct collections referred to as Dataset 1 and Dataset 2. Dataset 1 consists of 26 MRI slices of brain images, while Dataset 2 consists of 28 MRI slices of brain images, providing diverse imaging conditions for a comprehensive evaluation of our method. Figures 1 and 2 showcase examples of these images (specifically, slice 001 from Dataset 1 and slice 261 from Dataset 2), but our analysis extends beyond these individual slices.

For the statistical analysis presented in Table 1, we calculated metrics across a broad sample of slices from each dataset to ensure robustness and reliability. The term "per-slice" refers to individual MRI slices within each dataset, with slice numbers (e.g., 001, 261) indicating specific locations within the MRI volume. Additionally, we conducted repeated convergence runs during our experiments to verify the stability of our algorithm and ensure consistent results across various slices and datasets.

Our method achieved notable improvements in image quality, as demonstrated by Figures 1 and 2.

To objectively evaluate the effectiveness of our improved technique, we calculated the PSNR (Peak Signal-to-Noise Ratio) and conducted comparisons with both alternative approaches and enhanced versions of our own method.

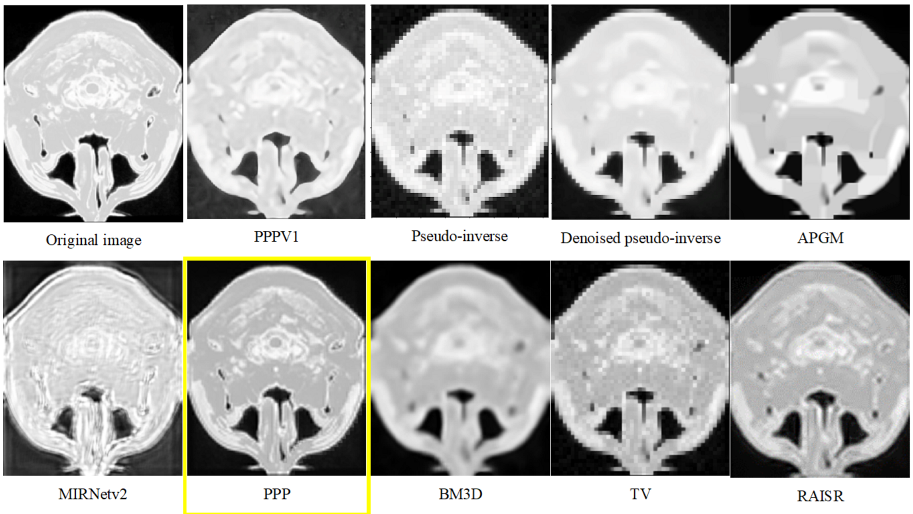

Figure 1. Result of image 001 from Dataset 1.

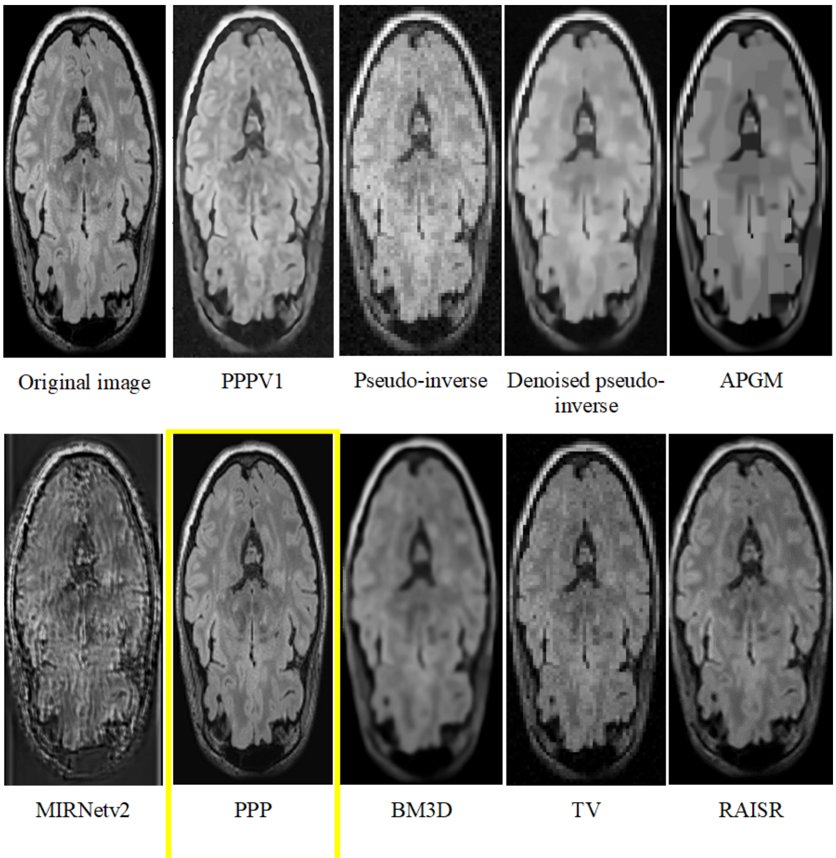

Figure 2. Result of image 261 from Dataset 2.

PSNR computes the peak signal-to-noise ratio between two images in decibels (dB). This ratio is a quality measurement between the original and the compressed image. PSNR can take values up to infinity; the higher the PSNR, the better the compressed image quality. Since the MRI exams in the TCIA dataset contain 16-bit images, in this case, the PSNR is computed as [27]:

$$\mathrm{PSNR} = 10\log_{10}\left(\frac{(2^{16}-1)^2}{MSE}\right) \quad (11)$$

where $MSE = \frac{\sum_{i=0}^{N-1}\sum_{j=0}^{M-1}(x(i,j) - \hat{x}(i,j))^2}{NM}$, with $x(i,j)$ and $\hat{x}(i,j)$ corresponding to the pixel value at position (I,j) of the ground truth x (original uncompressed image) and the compressed image $\hat{x}$ of dimensions $N \times M$, respectively. Note that the term $2^{16} - 1$ is the maximum pixel value in the input image data type.

Specifically, we compared against PPPV1 [18], APGM (Accelerated Proximal Gradient Method) [13], BM3D (block matching and 3D filtering) [16], total variation [14], RAISR (Rapid and Accurate Image Super-Resolution) [17] and MIRNetv2 [28], as well as with the pseudo-inverse and the denoised pseudo-inverse images. The difference between PPPV1 and the currently proposed method is that now we use a custom prior instead of DnCNN for the denoising, while we use the same rigid transformation. The outcomes, detailed in Table 1, demonstrate that our method surpasses others in delivering higher image quality. Finally, the runtime of our method per frame is 14 s, run in Google Colab with T4 GPU.

Table 1. PSNR statistics for the two datasets of all the methods.

	Dataset 1		**Dataset 2**	
	Average	**St.Dev**	**Average**	**St.Dev**
PPPV1	22.49	0.44	25.26	0.25
Pseudo-inverse	19.52	0.56	22.81	0.26
Denoised pseudo-inverse	20.36	0.51	23.73	0.28
APGM	19.91	0.34	23.78	0.22
MIRNetv2	14.05	0.27	14.26	0.18
PPP	**26.59**	0.49	25.67	0.65
BM3D	20.58	0.82	23.72	0.36
TV	22.48	0.44	23.50	0.29
RAISR	21.99	0.43	**25.77**	0.32

The Wilcoxon signed-rank test was used to compare the PSNR values of the proposed method with the respective values for PPP V1, Pseudo-inverse, Denoised Pseudoinverse, APGM, BM3D, and TV methods for Dataset 1. The results obtained with those statistical tests are shown in Figure 3 and indicate statistically significant differences between the PPP and the other six methods since no per-slice data were available for RAISR and MIRNetv2.

As for the subjective quality evaluation, it is based on the Natural Image Quality Evaluator (NIQE), which provides a score to assess the quality of images without requiring a reference. This no-reference quality metric is valuable because it does not need prior knowledge of specific types of image distortions or perceived degradation. NIQE works independently of any manually degraded data, which potentially makes it more adaptable to unexpected quality issues in images. A lower NIQE score suggests a higher perceptual quality of the image [29].

It is obvious from Table 2 that our method gives promising results. While the PPP method shows significant improvements over traditional SR techniques on most datasets, it does not outperform RAISR on Dataset 1 and provides only slight enhancements compared to PPPV1. This result may be attributed to the inherent characteristics of Dataset 1, such as lower noise levels, smoother image textures, and prominent edge orientations, which align well with RAISR's strengths. As noted in ref. [17], RAISR is a learning-based SR method that adapts its filters to local image features like gradients and edge orientations, offering computational efficiency and speed, which make it particularly effective for datasets with these characteristics. Additionally, the minimal performance difference between PPP and PPPV1 indicates that certain aspects of our proposed improvements may not fully leverage their potential under specific conditions. Taking these into consideration, we could say that the results demonstrate the robustness and effectiveness of our method in enhancing the natural quality of super-resolved videos for this specific dataset. It should be mentioned that for a lower upscaling factor (e.g., 2) the superiority of our method over the other ones was even greater.

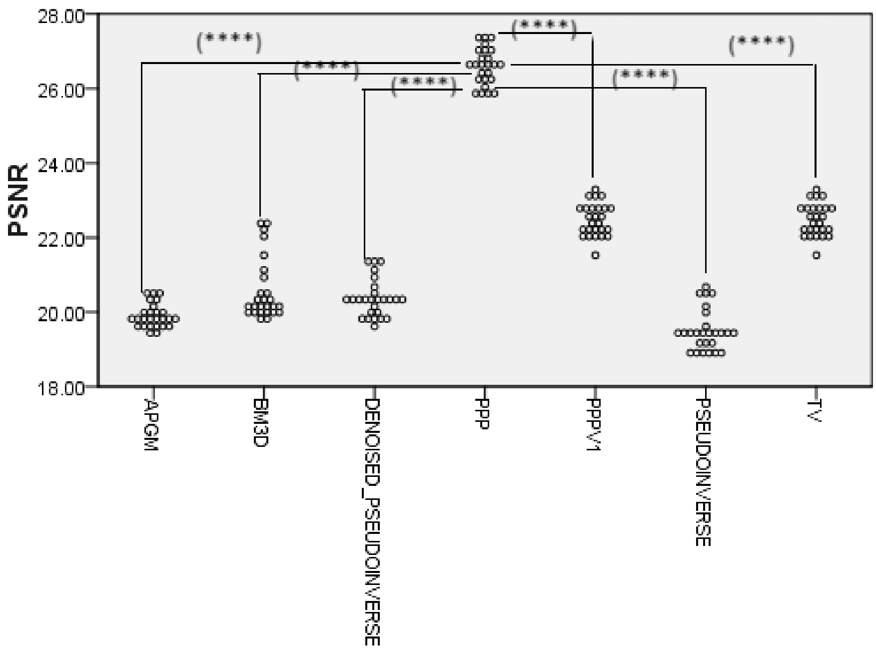

Figure 3. Scatter plot representation and the Wilcoxon signed-rank test results of the comparison for each of the six super-resolution methods (PPP V1, Pseudo-inverse, Denoised Pseudoinverse, APGM, BM3D and TV) with the PPP method regarding PSNR values for Dataset 1. Four stars (****) are less commonly used than one, two, or three asterisks in standard practice. The *p*-values were calculated using pairwise comparisons of the distributions, performed with MATLAB (version R2020a). A *p*-value close to zero, such as $p = 0.000$ or $p = 0.001$, is interpreted as statistically significant for this analysis but should not be overemphasized as an absolute correlation. Notably, RAISR and MIRNetv2 were excluded from these comparisons due to a lack of comparable data.

Table 2. NIQE statistics for the two datasets of all the methods.

	Dataset 1		**Dataset 2**	
	Average	**St.Dev**	**Average**	**St.Dev**
PPPV1	6.14	0.15	6.66	0.17
PPP	**5.82**	0.15	**6.39**	0.16
Pseudo-inverse	14.13	0.36	14.08	0.35
Denoised pseudo-inverse	14.13	0.36	14.08	0.35
APGM	13.86	0.35	13.03	0.33
BM3D	10.66	0.27	11.92	0.30
TV	12.22	0.31	12.82	0.32
RAISR	5.87	0.15	9.61	0.24
MIRNetv2	7.18	0.18	7.95	0.20

Visually, the PPP images exhibit several distinguishable enhancements. For instance, the edges are sharper and more defined, which is particularly evident when examining regions with high-frequency details. Additionally, the noise levels in the PPP images are noticeably reduced, maintaining the integrity of important structures. This results in a clearer depiction of fine details essential for accurate diagnosis. In comparison, images from conventional methods often display a trade-off between noise suppression and detail preservation, leading to either excessive smoothing or noise retention.

The segmented comparisons presented in Figures 4 and 5 highlight the visual performance of various super-resolution (SR) techniques, including the PPP method, in enhancing MRI image quality. Observing the segments, it is evident that the PPP method achieves a notable balance between detail preservation and noise reduction, demonstrating its superiority over other SR methods.

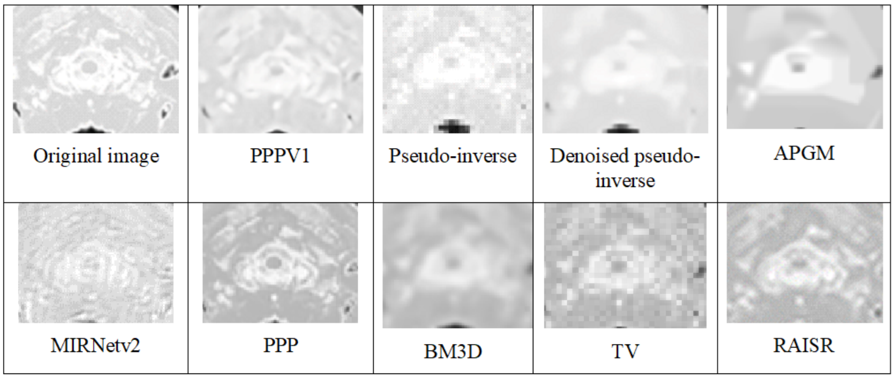

Figure 4. Segment of image 001 from Dataset 1.

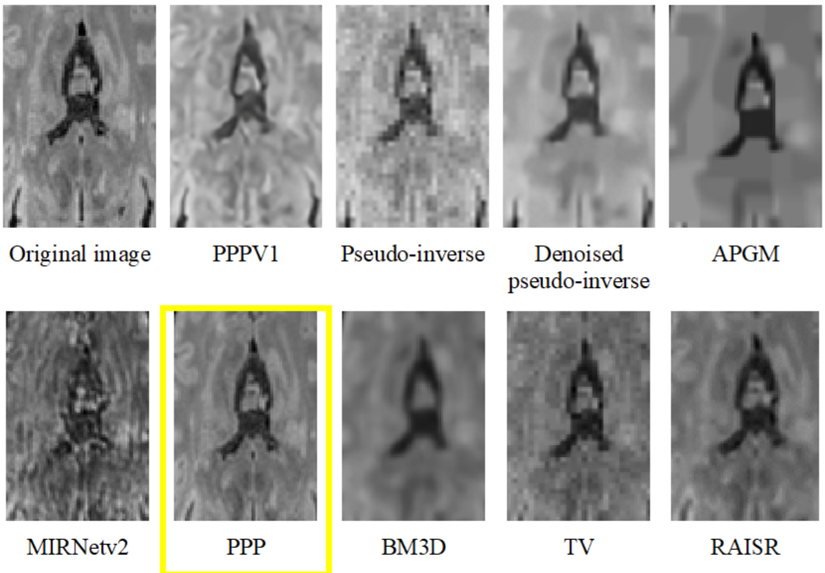

Figure 5. Segment of image 261 from Dataset 2.

4. Discussion

In summary, the results presented in this study highlight the superior performance of the proposed method in the field of video super-resolution. This method outperforms state-of-the-art techniques, as demonstrated by the substantial PSNR gains observed on the datasets used for evaluation. The following key takeaways can be drawn:

- The experimental results demonstrate the superiority of our approach over existing techniques, underscoring its potential for clinical applications in neuroimaging.
- The practical implications of our results suggest that our method holds great promise for applications where MRI slice quality enhancement is paramount.
- An advantage of our method lies in its computational simplicity. Unlike deep-neural-network-based methods, our approach does not rely on neural networks or require training, which reduces resource demands. However, we acknowledge that the runtime of our method per frame is 14 s, as measured on Google Colab with a T4 GPU.

While this runtime may not be suitable for real-time applications, it provides a balance between computational efficiency and the quality of the output, especially for tasks where real-time processing is not a critical requirement.

These findings make a strong case for the adoption of our method in MRI enhancement and upscaling tasks. We believe that the approach we suggest has the potential to contribute significantly to the field of video super-resolution and benefit a wide range of applications.

Author Contributions: Conceptualization, M.C.Z., G.C. and L.P.K.; methodology, M.C.Z., G.C. and L.P.K.; software, M.C.Z.; validation, M.C.Z., G.C. and L.P.K.; resources, M.C.Z., G.C. and L.P.K.; writing—original draft preparation, M.C.Z., G.C. and L.P.K.; writing—review and editing, M.C.Z., G.C. and L.P.K. All authors have read and agreed to the published version of the manuscript.

Funding: This research was funded by the project "Dioni: Computing Infrastructure for Big-Data Processing and Analysis" (MIS No. 5047222) co-funded by European Union (ERDF) and Greece through Operational Program "Competitiveness, Entrepreneurship and Innovation", NSRF 2014–2020.

Institutional Review Board Statement: Not applicable.

Informed Consent Statement: Not applicable.

Data Availability Statement: Availability of data and material: The datasets analyzed during the current study are available in the TCIA repository, https://www.cancerimagingarchive.net/ accessed on 13 October 2024.

Conflicts of Interest: The authors declare no conflicts of interest.

References

1. Aguena, M.L.S.; Mascarenhas, N.D.A.; Anacleto, J.C.; Fels, S.S. MRI Iterative Super Resolution with Wiener Filter Regularization. In Proceedings of the 2013 XXVI Conference on Graphics, Patterns and Images, Arequipa, Peru, 5–8 August 2013 .
2. Babu, M.G.; Panda, S.S.; Bandela, H.B. Super Resolution Image Reconstruction Using Iterative Regularization Method and Feed-Forward Neural Networks. *J. Phys. Conf. Ser.* **2019**, *1228*, 12021. [CrossRef]
3. Ahmadi, K.; Salari, E. *Edge-Preserving MRI Super Resolution Using a High Frequency Regularization Technique*; University of Toledo: Toledo, OH, USA, 2019.
4. Ben-Ezra, A.; Greenspan, H.; Rubner, Y. Regularized Super-Resolution of Brain MRI. In Proceedings of the 2009 IEEE International Symposium on Biomedical Imaging: From Nano to Macro, Boston, MA, USA, 28 June–1 July 2009.
5. Kawamura, N.; Yokota, T.; Hontani, H. Super-Resolution of Magnetic Resonance Images via Convex Optimization. *Int. J. Biomed. Imaging* **2018**, *2018*, 9262847. [CrossRef] [PubMed]
6. Peled, S.; Yeshurun, Y. Super-resolution in MRI: Application to human white matter fiber tract visualization by diffusion tensor imaging. *Magn. Reson. Med.* **2001**, *45*, 29–35. [CrossRef] [PubMed]
7. Scheffler, K. Super-resolution MRI: Strategies and applications. *NeuroImage* **2003**, *15*, 91–103.
8. Liu, C.; Sun, D.; On Bayesian Adaptive Video Super Resolution. *IEEE Trans. Pattern Anal. Mach. Intell.* **2014**, *36*, 346–360. [CrossRef]
9. Galatsanos, N.P.; Mesarović, V.Z.; Molina, R.; Katsaggelos, A.K. Hierarchical Bayesian image restoration from partially known blurs. *IEEE Trans. Image Process.* **2000**, *9*, 1784–1797. [CrossRef] [PubMed]
10. Zomet, A.; Rav-Acha, A.; Peleg, S. Robust super-resolution. In Proceedings of the 2001 IEEE Computer Society Conference on Computer Vision and Pattern Recognition, CVPR 2001, Kauai, HI, USA, 8–14 December 2001; Volume 1, pp. 645–650. [CrossRef]
11. Farsiu, S.; Robinson, D.; Elad, M.; Milanfar, P. Robust Shift and Add Approach to Super-Resolution. *Proc. Spie Int. Soc. Opt. Eng.* **2003**, *5203*, 121–130. [CrossRef]
12. Farsiu, S.; Robinson, M.D.; Elad, M.; Milanfar, P. Fast and robust multiframe super resolution. *IEEE Trans. Image Process.* **2004**, *13*, 1327–1344. [CrossRef]
13. Kamilov, U.S.; Bouman, C.A.; Buzzard, G.T.; Wohlberg, B. Plug-and-Play Methods for Integrating Physical and Learned Models in Computational Imaging: Theory, algorithms, and applications. *IEEE Signal Process. Mag.* **2023**, *40*, 85–97. [CrossRef]
14. Dabov, K.; Foi, A.; Katkovnik, V.; Egiazarian, K. Image restoration by sparse 3D transform-domain collaborative filtering. *Proc. Image Process. Algorithms Syst. VI* **2008**, *6812*, 681207. [CrossRef]
15. Gu, S.; Zhang, L.; Zuo, W.; Feng, X. Weighted Nuclear Norm Minimization with Application to Image Denoising. In Proceedings of the 2014 IEEE Conference on Computer Vision and Pattern Recognition (CVPR), Columbus, OH, USA, 23–28 June 2014; pp. 2862–2869. [CrossRef]
16. Rudin, L.I.; Osher, S.; Fatemi, E. Nonlinear total variation based noise removal algorithms. *Phys. Nonlinear Phenom.* **1992**, *60*, 259–268. [CrossRef]

17. Romano, Y.; Isidoro, J.; Milanfar, P. RAISR: Rapid and Accurate Image Super-Resolution. *IEEE Trans. Comput. Imaging* **2017**, *3*, 7744595. [CrossRef]
18. Zerva, M.C.; Kondi, L.P. Video super-resolution using Plug-and-Play priors. *IEEE Access* **2024**, *12*, 11963–11971. [CrossRef]
19. Park, S.C.; Park, M.K.; Kang, M.G. Super-resolution image reconstruction: A technical overview. *IEEE Signal Process. Mag.* **2003**, *20*, 21–36. [CrossRef]
20. Chantas, G.; Nikolopoulos, S.; Kompatsiaris, I. Heavy-Tailed Self-Similarity Modeling for Single Image Super Resolution. *IEEE Trans. Image Process.* **2020**, *30*, 838–852. [CrossRef]
21. Anjyo, K.; Ochiai, H. Rigid Transformation. In *Mathematical Basics of Motion and Deformation in Computer Graphics*, 2nd ed.; Springer International Publishing: Cham, Switzerland, 2017; pp. 5–21.
22. Szeliski, R. *Computer Vision: Algorithms and Applications*, 1st ed.; Springer: Berlin/Heidelberg, Germany, 2010; ISBN: 1848829345.
23. Kamilov, U.S.; Mansour, H.; Wohlberg, B. A Plug-and-Play priors approach for solving nonlinear imaging inverse problems. *IEEE Signal Process. Lett.* **2017**, *24*, 1872–1876. [CrossRef]
24. Chantas, G.K.; Galatsanos, N.P.; Woods, N.A. Super-resolution based on fast registration and maximum a posteriori reconstruction. *IEEE Trans. Image Process.* **2007**, *16*, 1821–1830. [CrossRef]
25. Balke, T.; Davis, F.R.; Garcia-Cardona, C.; McCann, M.; Pfister, L.; Wohlberg, B.E. Scientific Computational Imaging Code (SCICO). *J. Open Source Softw.* **2022**, *7*, 1898364. [CrossRef]
26. Clark, K.; Vendt, B.; Smith, K.; Freymann, J.; Kirby, J.; Koppel, P.; Moore, S.; Phillips, S.; Maffitt, D.; Pringle, M.; Tarbox, L. The Cancer Imaging Archive (TCIA): Maintaining and Operating a Public Information Repository. *J. Digit. Imaging* **2013**, *26*, 1045–1057. [CrossRef] [PubMed]
27. Raja, S.P.; Suruli, I.A. Image compression using WDR & ASWDR techniques with different wavelet codecs. *ACEEE Int. J. Inform. Technol.* **2011**, *1*, 23–26.
28. Zamir, S.W.; Arora, A.; Khan, S.H.; Munawar, H.; Khan, F.S.; Yang, M.H.; Shao, L. Learning Enriched Features for Fast Image Restoration and Enhancement. *IEEE Trans. Pattern Anal. Mach. Intell.* **2022**, *45*, 1934–1948. [CrossRef]
29. Wu, L.; Zhang, X.; Chen, H.; Wang, D.; ; Deng, J. VP-NIQE: An opinion-unaware visual perception natural image quality evaluator. *Neurocomputing* **2021**, *463*, 17–28. [CrossRef]